



# Intrinsic defect based homojunction: A novel quantum dots photoanode with enhanced charge transfer kinetics



Zhuofeng Hu<sup>b,c</sup>, Zhurui Shen<sup>a,b,c,\*</sup>, Jimmy C. Yu<sup>b,c,\*</sup>, Fangyi Cheng<sup>d,\*\*</sup>

<sup>a</sup> Key Laboratory of Advanced Ceramics and Machining Technology, Ministry of Education, School of Materials Science and Engineering, Tianjin University, Tianjin, 300072, PR China

<sup>b</sup> Department of Chemistry, The Chinese University of Hong Kong, Shatin, New Territories, Hong Kong, China

<sup>c</sup> Shenzhen Research Institute, The Chinese University of Hong Kong, Shenzhen, PR China

<sup>d</sup> Institute of New Energy Material Chemistry, Chemistry College, Key Laboratory of Advanced Energy Materials Chemistry (Ministry of Education), Chemistry College, Nankai University, Tianjin 300071, PR China

## ARTICLE INFO

### Article history:

Received 28 August 2016

Received in revised form 24 October 2016

Accepted 26 October 2016

Available online 29 October 2016

### Keywords:

Intrinsic defect

Quantum dots

Hematite

Photoanode

## ABSTRACT

Homojunctions are greatly beneficial to charge transfer. Their morphology, size and defect type determine their efficiency. Here, we diminish one component of the homojunction to as small as 5 nm by in-situ constructing a QDs-backbone hematite ( $\alpha\text{-Fe}_2\text{O}_3$ ) homojunction. This novel QDs-based homojunction is formed via intrinsic defects (mainly oxygen vacancies), which is totally different from most reported homojunctions based on extrinsic defects like external doping. With ultrahigh specific surface area, QDs contain sufficient high density of oxygen vacancies to generate “intrinsic” impurity energy levels and form a homojunction. Besides, the QDs better realize the potential of homojunction compared with other large-scale homojunctions, because their size are within the effective hole diffusion length. Charge carriers can easily migrate to the surface through a short distance (size of the QDs). Also, the QDs-backbone homojunction can overcome the shortcomings in previous QDs assembly and QDs based heterostructures due to less lattice mismatching. Therefore, the effective hole diffusion length  $L_p$  in the QDs- $\text{Fe}_2\text{O}_3$  (0.5–5.0 nm) becomes larger than that of  $\text{Fe}_2\text{O}_3$  (0.2–1.0 nm). Consequently, this homojunction shows pronounced enhancement in photoelectrochemical (PEC) performance. This work provides an alternative strategy to construct homojunctions via intrinsic defects and to rationally utilize QDs in PEC.

© 2016 Elsevier B.V. All rights reserved.

## 1. Introduction

Photoelectrochemical (PEC) water splitting is a promising strategy to convert solar energy into chemical fuels [1–10]. Charge transfer efficiency is one of the most important parameters for evaluating the performance of a PEC cell. It largely determines the utilization rate of photoexcited charges. In this regard, nanostructured photoelectrodes are helpful by shortening the charge carrier diffusion distance and increasing the specific surface area [11–14]. Among them, “Quantum dot” (QD) is an interesting nanostructured photoelectrodes. Its small size (<10 nm) are often within the effective charge carrier diffusion length. Its large specific surface area

can offer numerous reaction sites. These are dramatically advantageous to photoexcited charges to take part in water splitting prior to recombination [15]. Different QDs have been used in photoelectrodes including Sulfide QDs [16–19], Carbon QDs [20,21] and Graphene QDs [22,23]. However, the former need to be protected by sacrificial electrolyte like  $\text{Na}_2\text{S}$  and  $\text{Na}_2\text{SO}_3$ , while the latter are often vulnerable to oxidation at positive bias. It is still a challenge to fabricate high-efficient QDs-based photoelectrodes using more stable QDs, like  $\text{TiO}_2$ ,  $\text{ZnO}$  or  $\text{Fe}_2\text{O}_3$  etc.

Homojunction is the junction constructed by the same semiconductors with different band structures [24–27]. Compared with heterojunction, they are greatly beneficial to charge transfer due to little lattice mismatching and continuity of the chemical bonding [24]. Generally, homojunction is established via stepwise fabrication of the two components, and an appropriate band alignment between them is formed via extrinsic defects (external foreign atom doping) [26,27]. For example, Lee et al. firstly prepared a film of n-type  $\text{MoSe}_2$  and subsequently constructed a homojunction by depositing an p-type Nb-doped  $\text{MoSe}_2$  above [28]. However,

\* Corresponding authors at: Department of Chemistry, The Chinese University of Hong Kong, Shatin, New Territories, Hong Kong, China

\*\* Corresponding author.

E-mail addresses: [shenzhurui@tju.edu.cn](mailto:shenzhurui@tju.edu.cn) (Z. Shen), [jimyu@cuhk.edu.hk](mailto:jimyu@cuhk.edu.hk) (J.C. Yu), [fcheng@nankai.edu.cn](mailto:fcheng@nankai.edu.cn) (F. Cheng).

foreign dopants may have a deteriorating effect on charge transfer and separation in some conditions [4,29,30].

The morphology difference between the two components of homojunctions can play an important role in their performance [3,24,28]. The homojunctions have been established via two components with different morphologies, such as film/film [28], nanorod/films [3], and hexahedron prism/octahedronal etc [24]. For instance, Zou and coworkers have reported a CeO<sub>2</sub> homojunction based on the morphology difference of two components with different crystalline facets. An appropriate band alignment is formed between the prism surface of (100) facets and octahedron surface of (111) facets, thereby leading to efficient separation of photoexcited carriers and high photocatalytic activity [24].

However, there are few reports about the QDs-based homojunction. In our opinion, the homojunctions have some specific advantages when one component reaches the scale of several nanometers. In a PEC system, charge carriers generated in a photoelectrode need to cross the interface of solid electrode/liquid electrolyte, which is much more difficult than the interface of Ohm contact in dry electronic devices. Only those charge carriers generated near the interface can effectively contribute to PEC reaction. In case of photoanode, the effective distance is called effective hole diffusion length. Some frequently-used photoelectrode materials often suffer from very short effective hole diffusion length, such as hematite (several nm). In this regard, previous large-scale homojunction may limit their application in PECs.

Herein, in this regard, we have diminished the size of one component of the homojunction to as small as 5 nm by constructing a novel QDs-backbone hematite homojunction for PEC water oxidation. This QDs based homojunction displays interesting functional and structural advantages: (1) The unprecedent homojunction based on intrinsic defects (mainly oxygen vacancies) [31,32]. By reducing the size to QDs domain, the density of oxygen vacancies will reach a high enough level on the surface of QDs with ultrahigh surface area-to volume ratio. This can cause sufficient “intrinsic” impurity energy level in the forbidden band, thereby resulting in an appropriate band alignment between QDs and the backbone [31,32], which is totally different from most of the reported homojunctions based on extrinsic defects like external elemental doping. (Fig. 1a) (2) The QDs can better realize the potential of homojunction compared with other large-scale homojunctions due to its size within effective hole diffusion length of hematite. (3) The QDs-backbone homojunction can also overcome the shortcomings in QDs assembly and QDs based heterostructures due to less lattice mismatching [2,3,19,33,34]. The Fe<sub>2</sub>O<sub>3</sub> QDs based homojunction photoanode shows pronounced enhancement in PEC performance than the pristine Fe<sub>2</sub>O<sub>3</sub> photoanode. Its onset potential shifts negatively by 0.14 V and the photocurrent density increases by 4 times. The improved charge transfer is confirmed by a series of electrochemical analysis. Moreover, it also shows much better PEC performance than Fe<sub>2</sub>O<sub>3</sub> QDs assembly and Fe<sub>2</sub>O<sub>3</sub> QDs decorated photoanodes, respectively. Besides, compared with sulfide QDs that is vulnerable to photocorrosion, the Fe<sub>2</sub>O<sub>3</sub> QDs can work without protective electrolytes like Na<sub>2</sub>S and Na<sub>2</sub>SO<sub>3</sub> [35–37]. It preserves 90% of the initial photocurrent after 8000 s illumination.

## 2. Experimental

All chemical reagents are commercially available and used as received.

### 2.1. Preparation of Fe<sub>2</sub>O<sub>3</sub> nanorods on FTO glasses

70 mg of iron (III) chloride (FeCl<sub>3</sub>) and 140 mg of sodium sulfate (Na<sub>2</sub>SO<sub>4</sub>) was firstly dissolved in 20 mL of deionized (DI) water.

After 10 min of stirring, the solution was transferred into a 20 mL Teflon-lined stainless steel autoclave. A FTO glass substrate was cleaned ultrasonically in ethanol and acetone, and was placed into the autoclave, sealed and heated at 120 °C for 6 h. Thereafter, the FTO glass was taken out and washed with ethanol and water. A film of yellow FeOOH can be observed on the surface of the FTO glass. The film was then calcination at 800 °C for 10 min to transform FeOOH into Fe<sub>2</sub>O<sub>3</sub> and improve the contact with FTO.

### 2.2. Preparation of Fe<sub>2</sub>O<sub>3</sub> quantum dots/nanorods on FTO glasses (QDs-Fe<sub>2</sub>O<sub>3</sub>)

20 mg of glucose and 1.0 mL of ethanediamine were dissolved into 10 mL of distilled water to form a homogeneous solution. Subsequently, the pH of the solution was adjusted by adding different amount of 6 M hydrochloric acid. The solution was then transferred to a 25 mL Teflon-lined stainless steel autoclave. The Fe<sub>2</sub>O<sub>3</sub> NRs immersed into the solution, and heated at 210 °C for 10 h. After the reaction, the plate was taken out and washed with distilled water and ethanol before dried in a vacuum oven. Then, the plate was heated at 550 °C for 2 h at argon to improve the contact.

### 2.3. Preparation of Fe<sub>2</sub>O<sub>3</sub> QDs

2.0 mg of Iron (II) acetylacetone was firstly dissolved in 15 mL of absolute ethanol. After 10 min of stirring, the solution was transferred into a 20 mL Teflon-lined stainless steel autoclave for hydrothermal treatment at 200 °C for 16 h. The Fe<sub>2</sub>O<sub>3</sub> QDs were collected by centrifugation of the solution, and washed with ethanol and water for several times.

### 2.4. Preparation of QDs-assembly photoelectrode and QDs-decorated nanorod photoelectrode

A FTO glass substrate was cleaned ultrasonically in ethanol and acetone. The as-prepared Fe<sub>2</sub>O<sub>3</sub> QDs were suspended in ethanol and drop-coated on the FTO conducting glass. Then the glass was heated at 800 °C for 10 mins to enhance the crystallinity and contact with the substrate. Similarly, the Fe<sub>2</sub>O<sub>3</sub> QDs were decorated on the surface of Fe<sub>2</sub>O<sub>3</sub>nanorod arrays by the same method.

## 2.5. Materials characterization

Morphology of the products was characterized by scanning electron microscopy (SEM) on a FEI Quanta 400 microscope and by transmission electron microscopy (TEM) on a CM-120 microscope (Philips, 120 kV) coupled with an energy-dispersive X-ray (EDS) spectrometer (Oxford Instrument). X-ray diffraction (XRD) was performed on a Rigaku SmartLab X-ray diffractometer using Cu K $\alpha$  source irradiation ( $\lambda = 1.5406 \text{ \AA}$ ). Thermogravimetric analysis (TG) was recorded on a DTA1700 (PE, USA). The diffuse reflectance spectra (UV-vis) of the samples over a range of 300–2000 nm were recorded by a Hitachi U-4100 UV-vis system equipped with a Labsphere diffuse reflectance accessory. X-ray photoelectron spectroscopy (XPS) was performed using a Sengyang SKL-12 spectrometer equipped with a VG CLAM 4 MCD electron energy analyzer and twin anode Mg K $\alpha$  radiation (1253.6 eV) or Al K $\alpha$  radiation (1496.3 eV).

### 2.6. Photoelectrochemical measurements

Fe<sub>2</sub>O<sub>3</sub> NRs and Fe<sub>2</sub>O<sub>3</sub> QDs/RNs electrodes were fixed into the photoanodes by securing a copper wire onto a bare portion of the substrates via silver paste. All the photoelectrochemical measurements were performed in a three-electrode cell with a saturated-potassium-chloride silver electrode (Ag/AgCl)

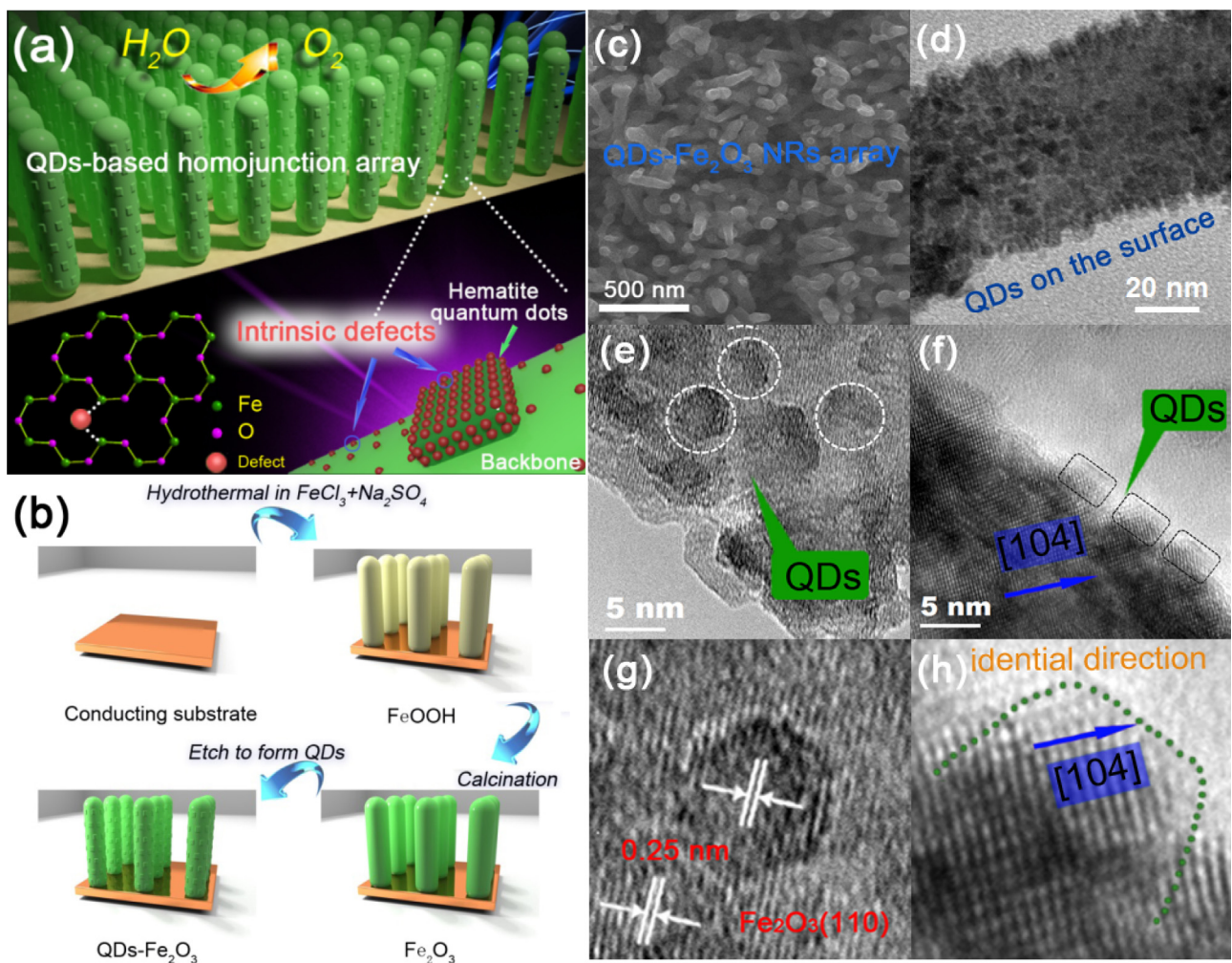


**Fig. 1.** (a) Schematic diagram of intrinsic defect based homojunction for photoelectrochemical water oxidation, (b) preparation process of QDs-Fe<sub>2</sub>O<sub>3</sub> homojunction, (c) the typical SEM image of QDs-Fe<sub>2</sub>O<sub>3</sub>, (d) the TEM image of a QDs-Fe<sub>2</sub>O<sub>3</sub> nanorod, (e) top-view and (f) side-view HRTEM images a QDs-Fe<sub>2</sub>O<sub>3</sub> nanorod, the circles in (e) and the boxes in (f) highlight the QDs, magnified HRTEM image (g) showing the identical crystal lattice spacing and (h) showing the identical crystal direction between the QDs and the backbone.

as a reference electrode, a platinum foil ( $1.0 \times 1.0 \text{ cm}^2$ ) as a counter electrode, and the Fe<sub>2</sub>O<sub>3</sub> NRs and Fe<sub>2</sub>O<sub>3</sub> QDs/RNs photoanodes as the working electrodes. The electrolyte was 1.0 M NaOH. Linear sweeps were measured by a CHI 660D electrochemical workstation. AC impedance measurements were conducted in the same configuration at different bias under simulated sunlight in the frequency range of  $10^6$ –0.1 Hz. The lifetime of electron was measured by plotting the Bode phase at open-circuit voltage. A 300 W xenon arc lamp coupled with an Air Mass (AM) 1.5 global filter ( $100 \text{ mW cm}^{-2}$ ) were used as the light source. The AM 1.5 global filter corrects the output of a xenon lamp to better match the solar spectrum with a  $37^\circ$  tilt angle. A series of band-pass light filters were also equipped onto the xenon arc lamp for incident photon-to-current efficiency (IPCE) measurements according to the equation:

$$\text{IPCE} = \frac{1240 \times I}{\lambda \times J_{\text{light}}} \times 100 \quad (1)$$

where  $I$  is the photocurrent density ( $\text{mA cm}^{-2}$ ),  $\lambda$  the incident light wavelength (nm), and  $J_{\text{light}}$  the power density of monochromatic light at a specific wavelength ( $\text{mW cm}^{-2}$ ). The Mott-Schottky plot is obtained according to the following equation:

$$\frac{1}{C^2} = \frac{2}{\varepsilon \cdot \varepsilon_0 \cdot e_0 \cdot N_D} (E - E_{FB} - \frac{kT}{e_0}) \quad (2)$$

where  $C$  is the space charge capacitance,  $\varepsilon$  and  $\varepsilon_0$  are the permittivity of the electrode and free space,  $e_0$  the elementary charge,  $A$  the electrochemical specific surface area,  $E$  the applied potential,  $E_{FB}$  the flat band potential,  $k$  the Boltzmann's Constant, and  $T$  the temperature.

### 3. Results and discussion

#### 3.1. Creating quantum dots on Fe<sub>2</sub>O<sub>3</sub> nanorods (QDs-Fe<sub>2</sub>O<sub>3</sub>)

In a typical synthesis (Fig. 1b), the Fe<sub>2</sub>O<sub>3</sub> nanorod array was prepared by calcinating a FeOOH array precursor. The as-prepared Fe<sub>2</sub>O<sub>3</sub> nanorod array was then hydrothermally treated in an acidic etching solution for a certain time. Since Fe<sub>2</sub>O<sub>3</sub> is slightly soluble in acidic solution, partial of the Fe<sub>2</sub>O<sub>3</sub> on the surface was etched after hydrothermal treatment. With an optimum initial pH value of 6.0, a layer of Fe<sub>2</sub>O<sub>3</sub> QDs was in-situ formed on the surface of the nanorods (sample denoted as "QDs-Fe<sub>2</sub>O<sub>3</sub>", see Fig. 1c–h).

As shown in Figs. 1 c,d and S1, the QDs-Fe<sub>2</sub>O<sub>3</sub> maintains its nanorod backbone. Some 5–6 nm tiny QDs are found on the surface of the nanorod (Fig. 1c,d). In the top-view HRTEM image, these darker QDs exist like platforms on the ground of nanorod (Fig. 1e, white circle region). A single QD is highlighted, and its crystal lattice is identical with that of the nanorod backbone (Fig. 1g). Both of

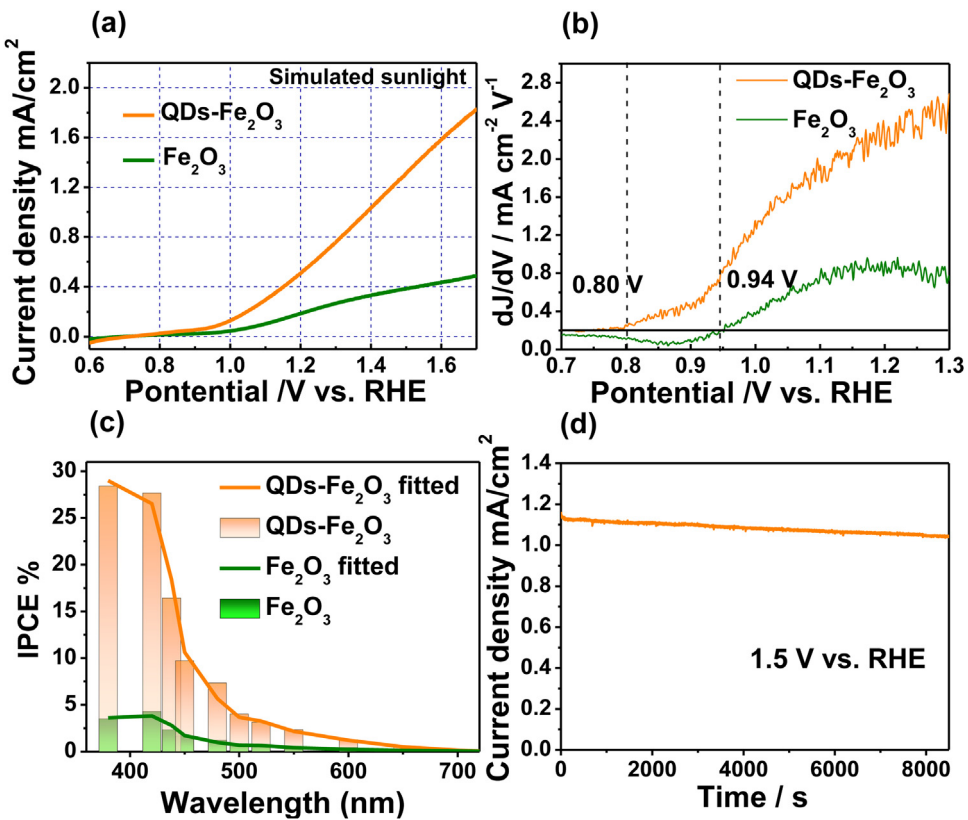


**Fig. 2.** (a) Voltammograms of  $\text{Fe}_2\text{O}_3$  (olive) and QDs- $\text{Fe}_2\text{O}_3$  (orange) under simulated sunlight (AM 1.5 G,  $100 \text{ mW cm}^{-2}$ ), the electrolyte is 1 M NaOH. (b) First order derivative of the photocurrent density as a function of potential, onset potential is defined as the potential at which  $dJ/dV > 0.2 \text{ mA cm}^{-2} \text{ V}^{-1}$ . (c) IPCE curves of  $\text{Fe}_2\text{O}_3$  and QDs- $\text{Fe}_2\text{O}_3$ . (d) Stability measurement of QDs- $\text{Fe}_2\text{O}_3$  at 1.5 V vs. RHE under simulated sunlight. (For interpretation of the references to color in this figure legend, the reader is referred to the web version of this article.)

them display the (110) crystal facets with the d-spacing of 0.25 nm. These indicate that the QDs are in-situ formed on the backbone of nanorods. There is no obvious lattice mismatching between  $\text{Fe}_2\text{O}_3$  QDs and its nanorod backbone, which is beneficial for charge transfer between them. This is further confirmed by the lateral view of HRTEM image. As shown in Fig. 1f and h, the lateral crystal facets and their aligned directions of QDs are also identical with those of nanorod backbone. The thickness of the QDs is 2–3 nm, while the diameter is 5–6 nm. Moreover, there is hardly any aggregations or overlap between adjacent QDs. This can prevent the “particle to particle” loss of charge transfer.

The XRD pattern of QDs- $\text{Fe}_2\text{O}_3$  resembles that of pristine  $\text{Fe}_2\text{O}_3$ . Both of them display the main diffraction peaks of  $\alpha\text{-Fe}_2\text{O}_3$  (JCPDS 33-0664) and the FTO substrates (Fig. S2) [38]. No other crystalline impurity can be found. This further confirms that the QDs on the surface of QDs- $\text{Fe}_2\text{O}_3$  have the same crystalline phase with that of nanorods. XPS analysis is conducted to study the chemical state of these QDs (Fig. S3). The Fe 2p spectrum of QDs- $\text{Fe}_2\text{O}_3$  shows a Fe 2p<sub>3/2</sub> peak centered at 711.4 eV and a Fe 2p<sub>1/2</sub> peak at ~724.5 eV, which are close to those of pristine  $\text{Fe}_2\text{O}_3$  and can be assigned to  $\text{Fe}^{3+}$  (Fig. S3a, b). The O 1s spectrum of QDs- $\text{Fe}_2\text{O}_3$  can be decomposed into two components after gaussian fitting (Fig. S3c). One is in 529.8 eV, corresponding to the oxygen atoms in the lattice [39]. The other is in 531.2 eV, indexing to oxygen atoms in the oxygen deficient region [39]. These values are also similar with those of pristine  $\text{Fe}_2\text{O}_3$  (Fig. S3d). Since the XPS signal mainly come from the QDs on surface, these results further confirm that the QDs on the surface are in the composition of  $\text{Fe}_2\text{O}_3$  [40].

### 3.2. Enhanced photoelectrochemical activity of QDs- $\text{Fe}_2\text{O}_3$ photoanode

The PEC performance of the QDs- $\text{Fe}_2\text{O}_3$  photoanode was evaluated by measuring the current-voltage (J-V) curves. The test (Figs. 2a and S4a) was performed in aqueous 1 M NaOH under AM 1.5 G simulated sunlight ( $100 \text{ mW cm}^{-2}$ ) and visible light ( $80 \text{ mW cm}^{-2}$ , UV cut-off). The measured potential versus the Ag/AgCl reference electrode ( $E_{\text{Ag}/\text{AgCl}}$ ) were converted to the reversible hydrogen electrode (RHE) scale according to the Nernst equation: [41–44]

$$E_{\text{RHE}} = E_{\text{Ag}/\text{AgCl}} + 0.059 \text{ pH} + E_{\text{Ag}/\text{AgCl}}^0 \quad (3)$$

The onset potential of a photoanode is often considered as the potential where PECs begin to generate noticeable photocurrent (Fig. 2a). Generally, it is defined as the potential where the rise of photocurrent exceeds  $0.2 \text{ mA cm}^{-2} \text{ V}^{-1}$  in the first order derivative of photocurrent against the potential (Fig. 2b) [45]. As shown in Fig. 2b, the pristine  $\text{Fe}_2\text{O}_3$  exhibits a late onset potential of 0.94 V vs. RHE. This is partially due to poor charge transfer in bulk  $\text{Fe}_2\text{O}_3$  and partially due to slow water oxidation kinetic (0.5 V overpotential, as shown in the J-V curve in the dark, Fig. S5). The onset potential of QDs- $\text{Fe}_2\text{O}_3$  shift negatively by 0.14 V–0.80 V vs. RHE. Since the QDs-covered electrode do not improve the water oxidation onset potential (Fig. S5). The improvement of 0.14 V should be ascribed to the enhancement of charge transfer in this homojunction photoanode. This is advantageous to the photoanode because it reduces the external electric power to driven the PEC process.

The photocurrent density of pristine  $\text{Fe}_2\text{O}_3$  then increases slowly and reaches a saturated value of  $0.4 \text{ mA cm}^{-2}$  (simulated sunlight, Fig. 2a) and  $0.3 \text{ mA cm}^{-2}$  (visible light, Fig. S4a) at 1.6 V vs.

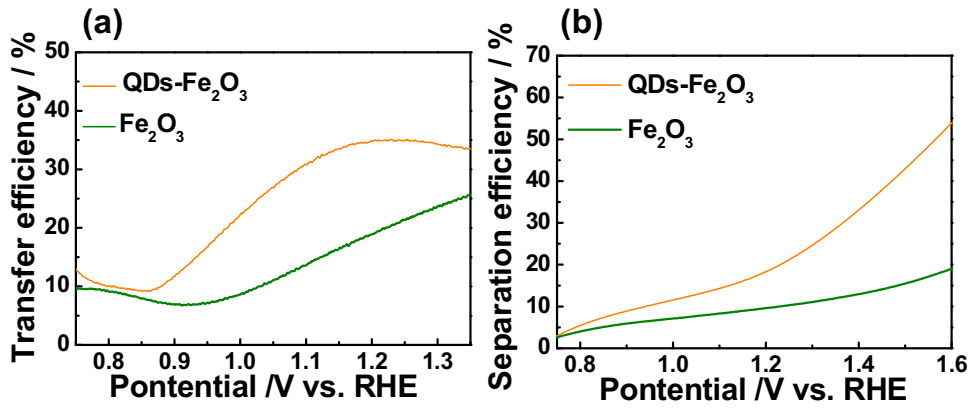


**Fig. 3.** (a) The transfer efficiency of  $\text{Fe}_2\text{O}_3$  and  $\text{QDs}-\text{Fe}_2\text{O}_3$  on their surface. (b) The separation efficiency of  $\text{Fe}_2\text{O}_3$  and  $\text{QDs}-\text{Fe}_2\text{O}_3$  inside their bulk part.

RHE. While that of  $\text{QDs}-\text{Fe}_2\text{O}_3$  increases much faster and reaches  $1.6 \text{ mA cm}^{-2}$  (simulated sunlight) and  $1.3 \text{ mA cm}^{-2}$  (visible light) at  $1.6 \text{ V}$  vs. RHE. These values are 4.0 (simulated sunlight) and 4.2 times (visible light) as high as that of  $\text{Fe}_2\text{O}_3$ , respectively. Notably, the J-V curve of the  $\text{QDs}-\text{Fe}_2\text{O}_3$  homojunction almost increases linearly and does not reach any plateau. It is better than some reported heterojunctions (e.g.,  $\text{CdS}-\text{TiO}_2$ ) that usually reaches a photocurrent plateau. This suggests an effective charge transfer in the  $\text{QDs}-\text{Fe}_2\text{O}_3$  homojunction photoanode [19,34,46].

The incident photon-to-current efficiency (IPCE) (Fig. 2c) of the  $\text{QDs}-\text{Fe}_2\text{O}_3$  is much higher than the pristine  $\text{Fe}_2\text{O}_3$ . After the wavelength of 550 nm, the IPCE of pristine  $\text{Fe}_2\text{O}_3$  dramatically drops to zero. While that of  $\text{QDs}-\text{Fe}_2\text{O}_3$  decays slowly until it reaches the low-energy threshold at 700 nm. This suggests that its PEC activity after 550 nm is mainly due to the excitation of QDs. However, the excitation of the QDs should not be the main reason for the enhanced PEC activity of  $\text{QDs}-\text{Fe}_2\text{O}_3$  because the IPCE values after 550 nm (1–2%) is much lower than its average IPCE value (Fig. S4b). Besides, the  $\text{QDs}-\text{Fe}_2\text{O}_3$  displays superior performance in stability (Fig. 2d). Its photocurrent maintains 92% of the initial maximum value after 8000 s illumination at  $1.5 \text{ V}$  vs. RHE. This can be ascribed to the in-situ growth of QDs, which immobilize and stabilize the QDs on the backbone by forming a continuous crystalline lattice between them and the backbone (Fig. 1g, h).

The PEC activities of the  $\text{QDs}-\text{Fe}_2\text{O}_3$  samples are greatly influenced by the initial pH value of the etching solution during the preparation. It can be adjusted by controlling the amount of hydrochloric acid and ethanediamine. The optimum pH value is 6.0, its corresponding sample is described in detail above (Figs. 1 and 2, S2–S5). At a higher pH value of 8.0, the  $\text{Fe}_2\text{O}_3$  nanorod is only slightly etched (Fig. S6a). The enhancement of photocurrent density is lower than that prepared at pH value of 6.0 (Fig. S6c). At a lower pH value of 3.0, the  $\text{Fe}_2\text{O}_3$  nanorod is heavily etched and some are even destroyed (Fig. S6b). Its photocurrent density also decreases compared with that prepared on the best condition (Fig. S6c).

### 3.3. Enhanced charge transfer kinetics of the $\text{QDs}-\text{Fe}_2\text{O}_3$ photoanode

Then, we measure the charge transfer efficiency on the surface ( $\eta_{\text{trans}}$ ) and charge separation efficiency inside the photoanode ( $\eta_{\text{sep}}$ ) by adding a fast hole scavenger to the electrolyte (details see Section S1) [47–49]. As shown in Fig. 3a, the  $\eta_{\text{trans}}$  of the  $\text{QDs}-\text{Fe}_2\text{O}_3$  begins to increase rapidly after  $0.85 \text{ V}$ , which is  $0.1 \text{ V}$  earlier than that of  $\text{Fe}_2\text{O}_3$ . This is similar with their photocurrent onset potentials (Fig. 2a, b). The  $\eta_{\text{trans}}$  of the  $\text{QDs}-\text{Fe}_2\text{O}_3$  also increases faster than that of  $\text{Fe}_2\text{O}_3$ , thereby confirming faster charge transfer on the

surface of  $\text{QDs}-\text{Fe}_2\text{O}_3$ . Similar with the  $\eta_{\text{trans}}$ , the  $\eta_{\text{sep}}$  of the  $\text{QDs}-\text{Fe}_2\text{O}_3$  is higher than that of  $\text{Fe}_2\text{O}_3$ , thereby confirming the higher separation efficiency inside its bulk counterpart (Fig. 3b).

The effective hole diffusion length ( $L_p$ ) of bare  $\text{Fe}_2\text{O}_3$  ranges between 0.5 to  $1.5 \text{ nm}$  (Figs. 4, S7, details in Section S2), which is consistent with previous reports [50,51]. When the applied bias increases, it is elongated due to wider depletion layer and stronger external driven force. However, it is still much smaller than the diameter of the nanorods ( $20\text{--}50 \text{ nm}$ ), indicating that only the periphery of the nanorod is effective, while the core of the nanorods suffer from serious recombination. On the contrary, in the presence of QDs, the  $L_p$  becomes larger with a range between 0.5 to  $5.0 \text{ nm}$  within all the potential window (Figs. 4, S7, details in Section S2). This relative larger  $L_p$  is close to the size of the QDs ( $2.0\text{--}5.0 \text{ nm}$ ), suggesting that most QDs could effectively contribute to the PEC performance.

Besides, the increased photovoltage ( $\Delta E_{\text{ph}}$ ) of  $\text{QDs}-\text{Fe}_2\text{O}_3$  ( $0.21 \text{ V}$  vs.  $0.15 \text{ V}$  of bare  $\text{Fe}_2\text{O}_3$ ) can also prove faster charge transfer of the  $\text{QDs}-\text{Fe}_2\text{O}_3$  photoanode (Fig. S8, Section S3) [52,53].

Subsequently, on the basis of microstructure and electrochemical study, we look insight into the mechanism of the superior performance for this novel homojunction, especially concerning on the effect of QDs introduction.

### 3.4. Analysis of superior performance for $\text{QDs}-\text{Fe}_2\text{O}_3$ photoanode: I, intrinsic defect based homojunction

We interestingly discover that the QDs-based homojunction is established via intrinsic defects in the QDs, an alternative strategy to build homojunctions. Intrinsic defect is formed when an atom

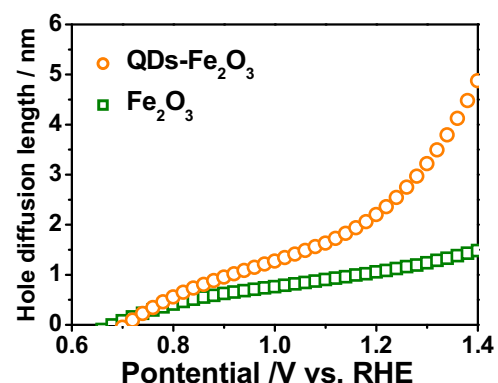


**Fig. 4.** The diagram of relationship between effective hole diffusion length  $L_p$  and applied bias in  $\text{Fe}_2\text{O}_3$  and  $\text{QDs}-\text{Fe}_2\text{O}_3$ .

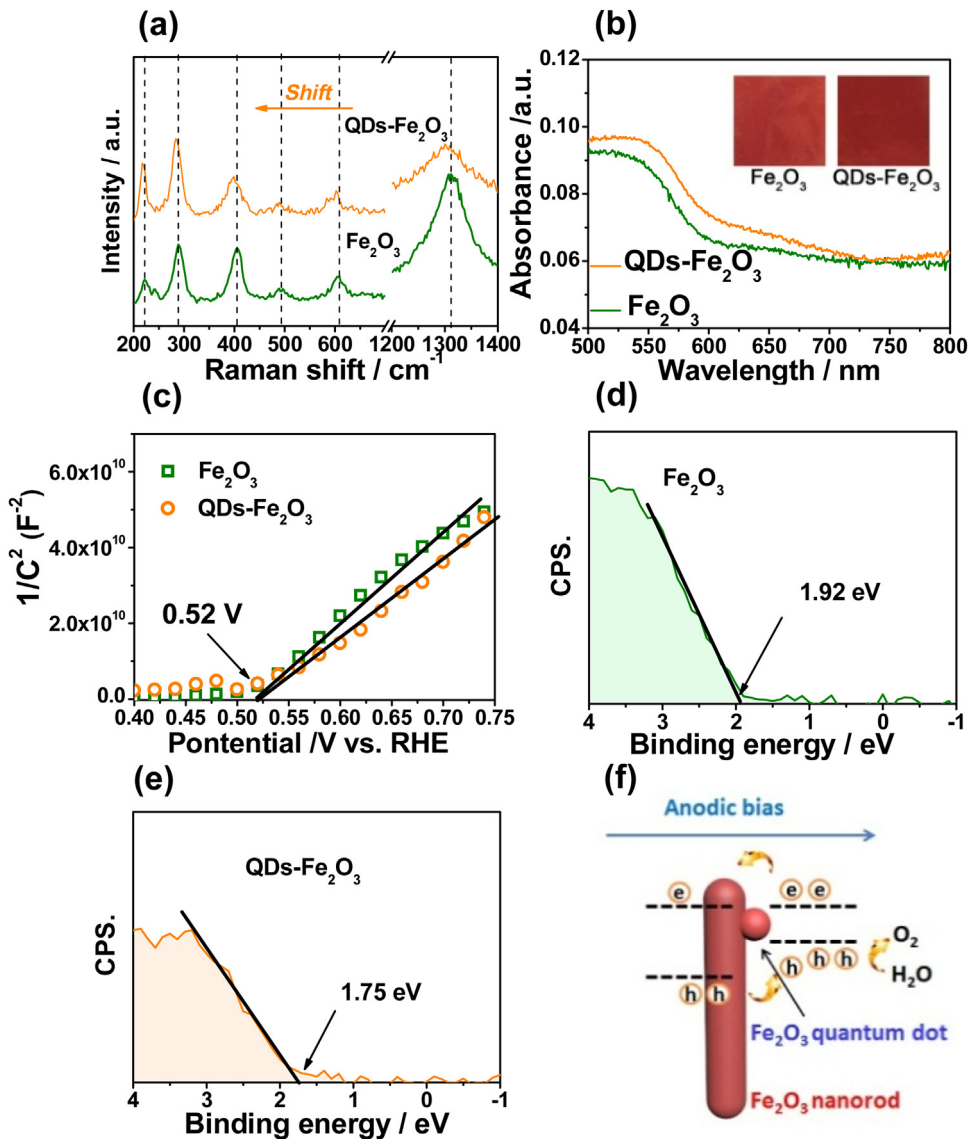


**Fig. 5.** (a) Raman spectra and (b) Optical image (inset), UV-vis diffuse spectra of pristine  $\text{Fe}_2\text{O}_3$  nanorod and QDs- $\text{Fe}_2\text{O}_3$  nanorod, (c) Mott-Schottky plot of  $\text{Fe}_2\text{O}_3$  (olive) and QDs- $\text{Fe}_2\text{O}_3$  (orange). Valence XPS spectrum of (d) QDs- $\text{Fe}_2\text{O}_3$  and (e)  $\text{Fe}_2\text{O}_3$ . (f) Energy diagram of QDs- $\text{Fe}_2\text{O}_3$ . (For interpretation of the references to color in this figure legend, the reader is referred to the web version of this article.)

is missing from a position that it ought to be in a crystal, which generates a vacancy, or formed when an atom occupies an interstitial sites where no atom would ordinarily appear, which generates a interstitialcy. In our case, the intrinsic defect is mainly the oxygen vacancy. For ionic compound, oxygen vacancies are often formed on the surface [31,32,54]. A theoretical model by Guisbiers suggests that at the nanoscale, a higher surface area to volume ratio will favor the formation of more vacancy defects on the surface [31,32]. When the density of vacancy defects is high enough, it would evidently change the density and nature of the states [55]. Specifically for oxygen vacancies in metal oxides, they can upward shift the valence band top, and higher density of oxygen vacancies lead to stronger shift [40].

In our design, via introduction of QDs, a nanostructure with ultrahigh specific surface area, we successfully bring sufficient high density of oxygen vacancies in the QDs component of the homojunction. Therefore, without any external atoms, we construct a new model of homojunction, which is totally different from previous homojunctions that are based on extrinsic defects. After the formation of QDs, the electrochemical active surface area (EASA) of

QDs- $\text{Fe}_2\text{O}_3$  increases by about 14.3 times from  $3.13 \text{ cm}^2$  to  $44.6 \text{ cm}^2$  geometric  $1 \text{ cm}^2$  (Fig. S9, Section S4). Meanwhile, the density of oxygen vacancies increases under the same preparation procedure. In the Raman spectrum of QDs- $\text{Fe}_2\text{O}_3$ , all the six peaks exhibit negative shift and wider width compared to that of  $\text{Fe}_2\text{O}_3$  (Fig. 5a, Table S1). It suggests an increasing amount of oxygen vacancies in the QDs according to literature [56–58]. While in its O 1s XPS spectrum (Fig. S3c), the peak of oxygen vacancy ( $531.4 \text{ eV}$ ) also increases after the formation of QDs. Moreover, the existence of oxygen vacancies is validated by electron spin resonance (ESR) spectra (Fig. S10). As is reported, the signal of oxygen vacancies are closer to that of free electrons ( $g = 2.0$ ) [59]. The signal at  $g = 1.95$  is associated with electrons trapped on oxygen vacancies [60]. The stronger signal in QDs- $\text{Fe}_2\text{O}_3$  confirms its higher density of oxygen vacancies. In our opinion, these oxygen vacancies rich QDs are structurally and functionally different from defect-free amorphous  $\text{FePO}_4$  coating layer in our previous report [54]. The QDs are also  $\text{Fe}_2\text{O}_3$  and they enhance the activity of  $\text{Fe}_2\text{O}_3$  photoanode mainly by promoting charge transfer, while the  $\text{FePO}_4$  coating layer mainly by suppressing the surface states.

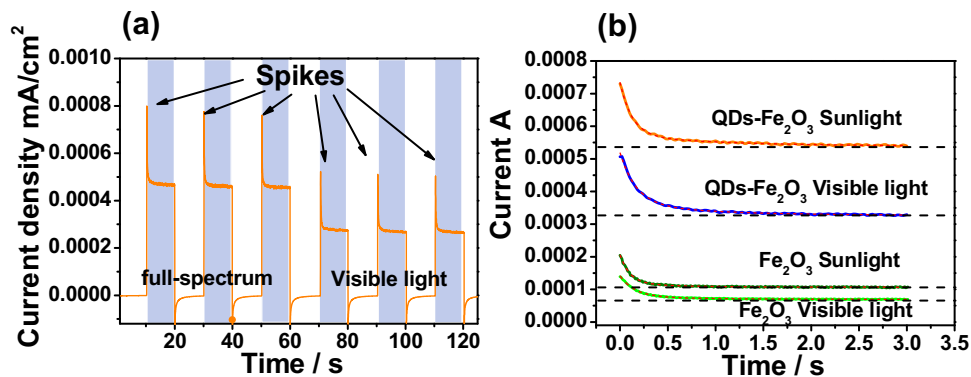


**Fig. 6.** (a) Some transient photocurrent spikes of QDs-Fe<sub>2</sub>O<sub>3</sub> observed upon chopped illumination. (b) Transient photocurrent decay profile of Fe<sub>2</sub>O<sub>3</sub> and QDs-Fe<sub>2</sub>O<sub>3</sub> under simulated sunlight and visible light at 1.23 V vs. RHE.

The high density of oxygen vacancies would evidently cause many “impurity level” in the forbidden band, and these “impurity level” result in a narrower band gap of QDs [40,55]. As shown in Fig. 5b (inset picture), the as-prepared QDs-Fe<sub>2</sub>O<sub>3</sub> is a little darker than the pristine Fe<sub>2</sub>O<sub>3</sub>. This is consistent with their UV-vis diffuse spectra (Fig. 5b). The spectrum of QDs-Fe<sub>2</sub>O<sub>3</sub> exhibits a slight red-shift compared with that of Fe<sub>2</sub>O<sub>3</sub>. Its corresponding Kubelka-Munk plot shows a band gap of 1.88 eV (Fig. S11a), which is narrower than that of Fe<sub>2</sub>O<sub>3</sub> (1.98 eV, Fig. S11b).

In the Mott-Schottky plot (Fig. 5c, Section S5), the flat band potentials ( $E_{FB}$ ) of both Fe<sub>2</sub>O<sub>3</sub> and QDs-Fe<sub>2</sub>O<sub>3</sub> are estimated to be 0.52 V vs. RHE [61–63]. It is known that the flat band potential is close to the Fermi level in a n-type semiconductor [64]. Thus, the conduction band of the QDs is hardly changed comparing to its bulk counterpart. According to the valence XPS spectrum (Fig. 5d, e) [65], the valence band of Fe<sub>2</sub>O<sub>3</sub> is 1.92 V below the Fermi level, which is consistent with previous report [66]. While the Fe<sub>2</sub>O<sub>3</sub> QDs exhibit a smaller value of 1.75 eV, indicating a higher valence band maximum. This is in good agreement with its narrower band gap, as shown in Fig. 5b, and suggests that the “impurity level” mainly locate above the valance band. This is similar with previous report of TiO<sub>2</sub> nanocrystals [40]. Overall, the band structure of the

QDs-Fe<sub>2</sub>O<sub>3</sub> homojunction can be obtained (Fig. 5f). Such a QDs-Fe<sub>2</sub>O<sub>3</sub> homojunction is favourable for charge separation and transfer. Photoexcited holes in the bulk core will preferentially transfer to the QDs with lower valence band via intimate contact in the homojunction. Then they and those holes generated in the QDs are easy to accumulate on the QDs. Therefore, such a homojunction photoanode has higher separation efficiency inside the photoanode (Fig. 3b).

The homojunction-induced enhanced charge separation can be reflected in the transient photocurrent measurement. As displayed in Fig. 6a, some transient photocurrent spikes are observed upon chopped illumination due to accumulation of photogenerated holes at the electrode/electrolyte interface. According to literature, this phenomenon is strongly related with bulk recombination [67]. Sample with serious recombination in the bulk hardly produces any spikes due to serious transfer loss in the bulk. However, similar spikes can still be observed in electrode after the formation of QDs. This suggests the as-prepared QDs-based homojunction has good charge separation efficiency. Also, after formation of QDs, both the decay kinetic time constants  $\tau_1$  and  $\tau_2$  increase under simulated sunlight or visible light, confirming the faster charge transfer in the bulk of QDs-Fe<sub>2</sub>O<sub>3</sub> (Fig. 6b, Table 1, details in Section S6).

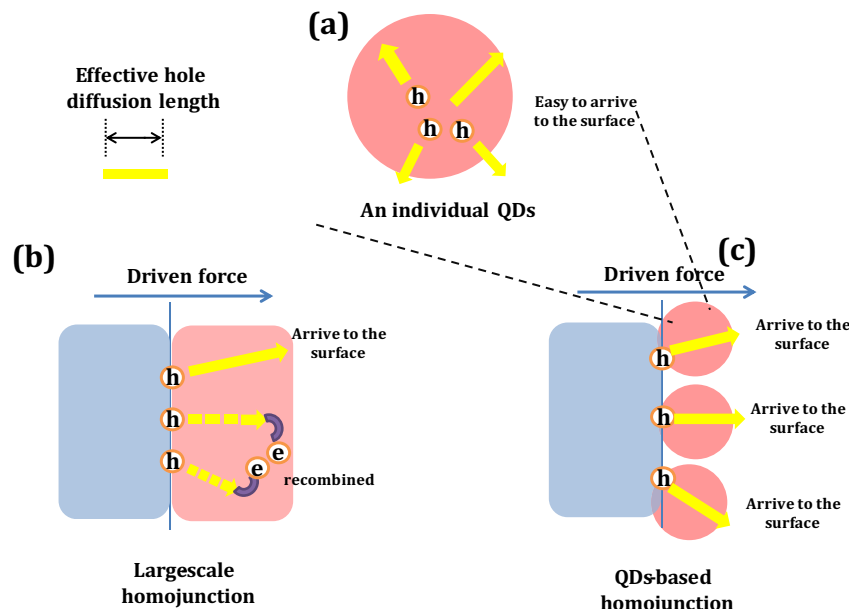


**Fig. 7.** The charge transfer kinetics in (a) an individual QD, (b) QDs-back bone homojunction and (c) large scale homojunction.

**Table 1**

The time constants  $\tau_1$  (fast),  $\tau_2$  (slow), total amount of accumulated charge (Q) and density of accumulated charge ( $Q_s$ ) for  $\text{Fe}_2\text{O}_3$  and QDs- $\text{Fe}_2\text{O}_3$  calculated from the decay profile of photocurrent.

	illumination	$\tau_1$ (s)	$\tau_2$ (s)	Q (C)	$Q_s (\text{C cm}^{-2})$
$\text{Fe}_2\text{O}_3$	Simulated sunlight	0.547	0.102	1.45E-05	1.25E-06
$\text{Fe}_2\text{O}_3$	Visible light	0.754	0.153	1.24E-05	1.15E-06
QDs- $\text{Fe}_2\text{O}_3$	Simulated sunlight	1.058	0.127	5.58E-05	4.65E-06
QDs- $\text{Fe}_2\text{O}_3$	Visible light	0.912	0.168	5.12E-05	3.97E-06

### 3.5. Analysis of superior performance for QDs- $\text{Fe}_2\text{O}_3$ photoanode: II, QDs-induced enhanced charge transfer

The QDs are superior to previous large-scale homojunctions in term of charge transfer when they are constructed in the QDs-backbone homojunction (Fig. 7). The QDs based homojunction shows much better charge transfer kinetics both on the surface and inside. On the surface, most region of the photoanode is covered with QDs (Fig. 1b,c). Under illumination, the majority of the QDs can be excited to generate photoexcited holes. It is known that the effective hole diffusion length (several nanometers) of hematite is close to the size of QDs. Therefore, in an individual QD, these photoexcited holes can easily reach the interface and contribute to PEC water oxidation (Fig. 7a), as supported by the faster charge transfer efficiency on the surface (Fig. 3a). This can be further confirmed by the slower surface recombination. As reflected in the decay profile of open circuit potential (Fig. 8, Section S7) [68], the pseudo-first order recombination rate constant ( $k$ ) in the presence of QDs ( $0.106 \text{s}^{-1}$ ) is about 8 times smaller than that of its QDs-free counterpart ( $0.919 \text{s}^{-1}$ ), suggesting suppression of surface recombination.

Inside the photoanode, the structure of QDs-backbone can take full advantage of the homojunction. As discussed above, the main function of a homojunction is to promote charge separation via appropriate band alignment. Specifically for PECs, the homojunction should facilitate the migration of photoexcited holes to the surface for water oxidation. For homojunctions with two large-scale components, the holes must pass through a long distance to reach the surface, and are vulnerable to recombination with electrons (Fig. 7b). This will be more pronounced for materials with short effective hole diffusion length like hematite in this work. However, in our QDs-backbone homojunction, more holes can survive from recombination and efficiently contribute to the photocatalytic reaction. This is because they only pass through a relative short distance (several nanometers), which is within the effective hole diffusion length of hematite (Fig. 7c). Also, with high specific surface area (Fig. S9), QDs often have high density of active sites on the surface, which is also beneficial to the PEC reactions

relative to large-scale materials. Consequently, these two reasons help QDs take full advantage of the homojunction.

The enhanced charge transfer kinetic can be confirmed by the total amount of charge stored in the surface states (denoted as Q), which is obtainable by integrating the photocurrent transients (Fig. S12, violet region) [69]. The density of accumulated charge per  $\text{cm}^2$  ( $Q_s$ ) is obtained by driving Q with the specific surface area (Fig. S9). Results show that the density of accumulated charge (holes for photoanode) of QDs- $\text{Fe}_2\text{O}_3$  is about four times lower than that of  $\text{Fe}_2\text{O}_3$  (Table 1). Associated with the fact that the amount of holes arriving the interface (photocurrent density) is much higher for QDs- $\text{Fe}_2\text{O}_3$ , the charge transfer efficiency at the interface of QDs- $\text{Fe}_2\text{O}_3$  is much higher than that in  $\text{Fe}_2\text{O}_3$ . This is consistent with the other evidence of enhanced surface charge transfer (Figs. 3 a, 8).

### 3.6. Analysis of superior performance for QDs- $\text{Fe}_2\text{O}_3$ photoanode: III, structural advantage of QDs-based homojunction

Finally, we discuss the structural advantage of QDs-homojunction compared with other QDs based photoanodes. Previously, direct preparation of QDs-assembly photoelectrodes is the first strategy for the application of QDs in PECs [2,3,19,33]. In an individual QD, the charge transfer to the electrolyte has been proved to be highly effective. However, the charge transfer among different QDs in the photoelectrode is usually difficult due to the large area of “particle to particle” interfaces (Fig. 9a) [70]. This results in a low photocurrent density with the magnitude of  $\text{nA cm}^{-2}$  or  $\mu\text{A cm}^{-2}$  for most reported QDs-assembly photoelectrodes [21,33,71,72].

Another strategy is to uniformly immobilize a layer of QDs on a semiconductor backbone as the support, like  $\text{TiO}_2$  and  $\text{ZnO}$  [16,17,19]. This can reduce charge transfer loss at the “particle to particle” interfaces and enhance the PEC performance. To date, related studies mainly focus on sensitization of wide-bandgap metal oxide photoelectrodes (like  $\text{TiO}_2$  and  $\text{ZnO}$ ) by sulfide QDs [17,19,37], graphene QDs [20] and carbon QDs etc [22,23]. However, they often contain many lattice mismatching and junction defects at the interfaces of “particle to backbone” (Fig. 9c) [24], thereby resulting in unwanted charge transfer loss. For example, some  $\text{CdS}$  QDs or  $\text{CdSe}$  QDs sensitized photoanodes will reach a saturated plateau photocurrent after a certain positive bias due to limited charge transfer between the QDs and the metal oxides [19,34]. Therefore, rational design of interfaces contact is very important for the application of QDs in PECs.

Herein, we performed two additional experiments to confirm the better interface contact of homojunction.  $\text{Fe}_2\text{O}_3$  quantum dots are prepared by a hydrothermal method (Experimental section) and deposited on a conducting FTO glass (Fig. S13a). Such a QDs-assembly photoelectrode exhibits an early onset potential at about 0.7 V, but shows a very weak photocurrent density on the magnitude of  $10^{-2} \text{ mA cm}^{-2}$  (Fig. 9b). This should be mainly due to the charge transfer loss at the “particle to particle” interface (Fig. 9a). We also deposit the  $\text{Fe}_2\text{O}_3$  QDs on the  $\text{Fe}_2\text{O}_3$  nanorod arrays (Figs. 9 c, S13b). The photocurrent only increase by about 20% (Fig. 9d), which is much smaller than that of the QDs- $\text{Fe}_2\text{O}_3$  homojunction due to relative poor charge transfer at the “particle to backbone” interface. Also, the charge transfer loss in the bulk of these two photoelectrodes can be reflected in the absence of photocurrent spikes under chopped illumination (Figs. S14, 6 a). These two experiments confirm that the homojunction structure is more favorable for the QDs based photoanode.

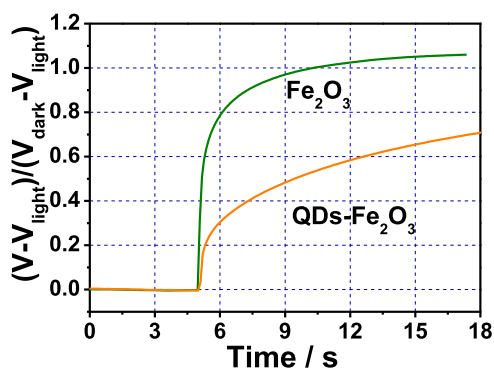
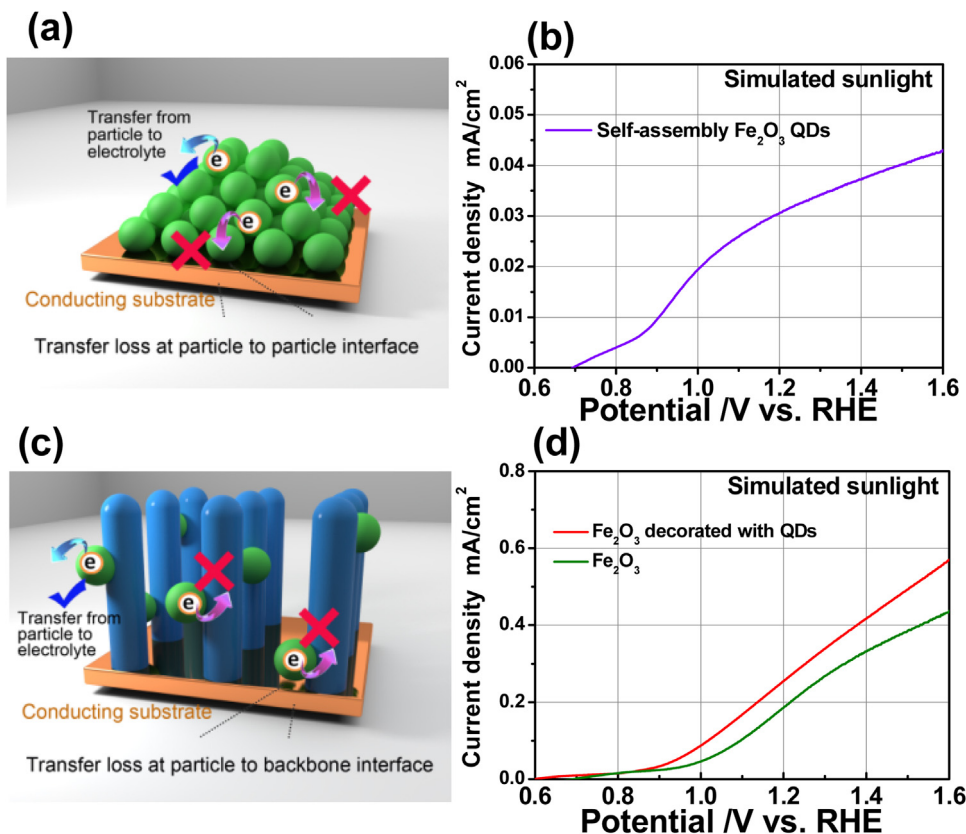


Fig. 8. Normalized open-circuit potential ( $V_{oc}$ ) decay curves after turning off the simulated sunlight.



**Fig. 9.** (a) The diagram and (b) Voltammograms of self-assembly  $\text{Fe}_2\text{O}_3$  QDs (c) the diagram of  $\text{Fe}_2\text{O}_3$  decorated with QDs and (d) Voltammograms of  $\text{Fe}_2\text{O}_3$  with (orange) and without (olive) QDs. (For interpretation of the references to color in this figure legend, the reader is referred to the web version of this article.)

#### 4. Conclusions

In summary, we demonstrate a novel strategy to enhance charge transfer for QDs based photoelectrodes by constructing a hematite “QDs-backbone homojunction”. This novel QDs-based homojunction is established via intrinsic defects (mainly oxygen vacancies), which is totally different from previous homojunctions on the basis of extrinsic defect. With excellent charge transfer kinetics, the QDs can better realize the potential of homojunction compared with other large-scale homojunctions. The QDs-backbone homojunction can also overcome the shortcomings in QDs assembly and QDs based heterostructures due to less lattice mismatching. It shows enhanced PEC activity than those of the pristine  $\text{Fe}_2\text{O}_3$  photoanode, self-assembly  $\text{Fe}_2\text{O}_3$  QDs and  $\text{Fe}_2\text{O}_3$  QDs decorated  $\text{Fe}_2\text{O}_3$  photoanodes, respectively. Its enhanced charge transfer kinetics is analyzed by spectroscopic electrochemical study. This work offered an alternative strategy for construction of homojunction by creating Intrinsic defects, e.g. oxygen and other vacancies, dislocation or crystalline distort etc. Moreover, it paved a new way for rational utilization of QDs in PECs. In addition, this strategy can also be expanded to generate quantum dots on other metal oxide photoanodes. Probably, these include  $\text{TiO}_2$ ,  $\text{WO}_3$  and  $\text{ZnO}$  etc.

#### Acknowledgements

The work described in this paper was partially supported by the Shenzhen Basic Research Scheme (JCYJ20120619151417947) and two grants from the Research Grants Council of the Hong Kong Special Administrative Region, China. (Project No. T23-407/13-N and Project No. 14304315). This work was also supported by the National Natural Science Foundation of China (Ref. No. 21173179, Ref. No. 21303118) and a grant from the Vice-Chancellor's One-off

Discretionary Fund of The Chinese University of Hong Kong (Project No. VCF2014016).

#### Appendix A. Supplementary data

Supplementary data associated with this article can be found, in the online version, at <http://dx.doi.org/10.1016/j.apcatb.2016.10.079>.

#### References

- [1] Z. Chen, H. Dinh, E. Miller, Photoelectrochemical Water Splitting: Standards, Experimental Methods, and Protocols, 2013.
- [2] Y. Jin, D.H. Keum, S.-J. An, J. Kim, H.S. Lee, Y.H. Lee, *Adv. Mater.* 27 (2015) 5534–5540.
- [3] P.-J. Li, Z.-M. Liao, X.-Z. Zhang, X.-J. Zhang, H.-C. Zhu, J.-Y. Gao, K. Laurent, Y. Leprince-Wang, N. Wang, D.-P. Yu, *Nano Lett.* 9 (2009) 2513–2518.
- [4] M.K. Nowotny, T. Bak, J. Nowotny, C.C. Sorrell, *Phys. Status Solidi (b)* 242 (2005) R88–R90.
- [5] S. Yang, X. Feng, X. Wang, K. Müllen, *Angew. Chem. Int. Ed.* 50 (2011) 5339–5343.
- [6] R. Asahi, T. Morikawa, T. Ohwaki, K. Aoki, Y. Taga, *Science* 293 (2001) 269.
- [7] J.C. Yu, L. Zhang, Z. Zheng, J. Zhao, *Chem. Mater.* 15 (2003) 2280–2286.
- [8] R. Zheng, L. Lin, J. Xie, Y. Zhu, Y. Xie, *J. Phys. Chem. C* 112 (2008) 15502–15509.
- [9] Y. Tian, H. Sang, X. Wang, *Chin. J. Catal.* 33 (2012) 1395–1401.
- [10] M. Iwase, K. Yamada, T. Kurisaki, B. Ohtani, H. Wakita, *Appl. Catal. B* 140–141 (2013) 327–332.
- [11] Y. Qiu, S.-F. Leung, Q. Zhang, B. Hua, Q. Lin, Z. Wei, K.-H. Tsui, Y. Zhang, S. Yang, Z. Fan, *Nano Lett.* 14 (2014) 2123–2129.
- [12] D.A. Wheeler, G. Wang, Y. Ling, Y. Li, J.Z. Zhang, *Energy Environ. Sci.* 5 (2012) 6682–6702.
- [13] Y. Xu, W. Zhao, M. Feng, H. Sang, *Environ. Chem.* 33 (2014) 129–134.
- [14] M. Iwase, K. Yamada, T. Kurisaki, O.O. Prieto-Mahaney, B. Ohtani, H. Wakita, *Appl. Catal. B* 132–133 (2013) 39–44.
- [15] D. Chandra, K. Saito, T. Yui, M. Yagi, *Angew. Chem. Int. Ed.* 52 (2013) 12606–12609.
- [16] K. Wang, S. Wan, Q. Liu, N. Yang, J. Zhai, *RSC Adv.* 3 (2013) 23755–23761.

- [17] S. Kelkar, C. Ballal, A. Deshpande, S. Warule, S. Ogale, *J. Mater. Chem. A* 1 (2013) 12426–12431.
- [18] L. Korala, Z. Wang, Y. Liu, S. Maldonado, S.L. Brock, *ACS Nano* 7 (2013) 1215–1223.
- [19] B. Liu, X.B. Li, Y.J. Gao, Z.J. Li, Q.Y. Meng, C.H. Tung, L.Z. Wu, *Energy Environ. Sci.* 8 (2015) 1443–1449.
- [20] C.X. Guo, Y. Dong, H.B. Yang, C.M. Li, *Adv. Energy Mater.* 3 (2013) 997–1003.
- [21] K.-A. Tsai, Y.-J. Hsu, *Appl. Catal. B* 164 (2015) 271–278.
- [22] M.X. Sun, X.Q. Ma, X. Chen, Y.J. Sun, X.L. Cui, Y.H. Lin, *RSC Adv.* 4 (2014) 1120–1127.
- [23] X. Zhang, H. Huang, J. Liu, Y. Liu, Z.H. Kang, *J. Mater. Chem. A* 1 (2013) 11529–11533.
- [24] P. Li, Y. Zhou, Z. Zhao, Q. Xu, X. Wang, M. Xiao, Z. Zou, *J. Am. Chem. Soc.* 137 (2015) 9547–9550.
- [25] Z.R. Shen, Z.F. Hu, W.J. Wang, S.F. Lee, D.K.L. Chan, Y.C. Li, T. Gu, J.C. Yu, *Nanoscale* 6 (2014) 14163–14167.
- [26] Z.F. Hu, J.C. Yu, *J. Mater. Chem. A* 1 (2013) 12221–12228.
- [27] Z.F. Hu, J.C. Yu, T. Ming, J.F. Wang, *Appl. Catal. B-Environ.* 168 (2015) 483–489.
- [28] Z.F. Hu, Z.R. Shen, J.C. Yu, *Chem. Mater.* 28 (2016) 564–572.
- [29] S. Wang, L. Pan, J.-J. Song, W. Mi, J.-J. Zou, L. Wang, X. Zhang, *J. Am. Chem. Soc.* 137 (2015) 2975–2983.
- [30] X. Li, S. Wu, P. Hu, X. Xing, Y. Liu, Y. Yu, M. Yang, J. Lu, S. Li, W. Liu, *J. Appl. Phys.* 106 (2009) 043913.
- [31] Z.F. Hu, Z.X. Yan, P.K. Shen, C.J. Zhong, *Nanotechnology* 23 (2012) 10.
- [32] Z.F. Hu, C. Chen, H. Meng, R.H. Wang, P.K. Shen, H.G. Fu, *Electrochem. Commun.* 13 (2011) 763–765.
- [33] M. Hojeij, B. Su, S.X. Tan, G. Meriguet, H.H. Girault, *ACS Nano* 2 (2008) 984–992.
- [34] H. Wang, G. Wang, Y. Ling, M. Lepert, C. Wang, J.Z. Zhang, Y. Li, *Nanoscale* 4 (2012) 1463–1466.
- [35] G. Wang, X. Yang, F. Qian, J.Z. Zhang, Y. Li, *Nano Lett.* 10 (2010) 1088–1092.
- [36] J.H. Bang, P.V. Kamat, *ACS Nano* 5 (2011) 9421–9427.
- [37] W. Sheng, B. Sun, T. Shi, X. Tan, Z. Peng, G. Liao, *ACS Nano* 8 (2014) 7163–7169.
- [38] Y. Ling, G. Wang, D.A. Wheeler, J.Z. Zhang, Y. Li, *Nano Lett.* 11 (2011) 2119–2125.
- [39] G.D. Khattak, A. Mekki, M.A. Gondal, *J. Phys. Chem. Solids* 74 (2013) 13–17.
- [40] L. Li, J. Yan, T. Wang, Z.-J. Zhao, J. Zhang, J. Gong, N. Guan, *Nat. Commun.* 6 (2015).
- [41] M. Xu, P.M. Da, H.Y. Wu, D.Y. Zhao, G.F. Zheng, *Nano Lett.* 12 (2012) 1503–1508.
- [42] S. Hoang, S.W. Guo, N.T. Hahn, A.J. Bard, C.B. Mullins, *Nano Lett.* 12 (2012) 26–32.
- [43] T. Minegishi, N. Nishimura, J. Kubota, K. Domen, *Chem. Sci.* 4 (2013) 1120–1124.
- [44] Y. Ma, S.R. Pendlebury, A. Reynal, F. Le Formal, J.R. Durrant, *Chem. Sci.* 5 (2014) 2964–2973.
- [45] C. Du, X. Yang, M.T. Mayer, H. Hoyt, J. Xie, G. McMahon, G. Bischoping, D. Wang, *Angew. Chem. Int. Ed.* 52 (2013) 12692–12695.
- [46] L.P. Liu, G.M. Wang, Y. Li, Y.D. Li, J.Z. Zhang, *Nano Res.* 4 (2011) 249–258.
- [47] P.M. Rao, L. Cai, C. Liu, I.S. Cho, C.H. Lee, J.M. Weisse, P. Yang, X. Zheng, *Nano Lett.* 14 (2014) 1099–1105.
- [48] G. Liu, J. Shi, F. Zhang, Z. Chen, J. Han, C. Ding, S. Chen, Z. Wang, H. Han, C. Li, *Angew. Chem. Int. Ed.* 53 (2014) 7295–7299.
- [49] K.M.H. Young, B.M. Klahr, O. Zandii, T.W. Hamann, *Catal. Sci. Technol.* 3 (2013) 1660–1671.
- [50] G.M. Wang, Y.C. Ling, D.A. Wheeler, K.E.N. George, K. Horsley, C. Heske, J.Z. Zhang, Y. Li, *Nano Lett.* 11 (2011) 3503–3509.
- [51] J.H. Kennedy, K.W. Frese, *J. Electrochem. Soc.* 125 (1978) 709–714.
- [52] A.C. Chen, S. Nigro, *J. Phys. Chem. B* 107 (2003) 13341–13348.
- [53] V. Subramanian, E. Wolf, P.V. Kamat, *J. Phys. Chem. B* 105 (2001) 11439–11446.
- [54] Z. Hu, Z. Shen, J.C. Yu, *Chem. Mater.* 28 (2016) 564–572.
- [55] Z.X. Yan, Z.F. Hu, C. Chen, H. Meng, P.K. Shen, H.B. Ji, Y.Z. Meng, *J. Power Sources* 195 (2010) 7146–7151.
- [56] X.H. Lu, Y.X. Zeng, M.H. Yu, T. Zhai, C.L. Liang, S.L. Xie, M.S. Balogun, Y.X. Tong, *Adv. Mater.* 26 (2014) 3148–3155.
- [57] D.L.A. deFaria, S.V. Silva, M.T. deOliveira, *J. Raman Spectrosc.* 28 (1997) 873–878.
- [58] X.Y. Pan, X.M. Ma, *J. Solid State Chem.* 177 (2004) 4098–4103.
- [59] F. Dong, X. Xiao, G. Jiang, Y. Zhang, W. Cui, J. Ma, *Phys. Chem. Chem. Phys.* 17 (2015) 16058–16066.
- [60] A.B. Djurišić, W.C.H. Choy, V.A.L. Roy, Y.H. Leung, C.Y. Kwong, K.W. Cheah, T.K. Gundu Rao, W.K. Chan, H. Fei Lui, C. Surya, *Adv. Funct. Mater.* 14 (2004) 856–864.
- [61] X.Y. Yang, A. Wolcott, G.M. Wang, A. Sobo, R.C. Fitzmorris, F. Qian, J.Z. Zhang, Y. Li, *Nano Lett.* 9 (2009) 2331–2336.
- [62] C. Baumanis, D.W. Bahnemann, *J. Phys. Chem. C* 112 (2008) 19097–19101.
- [63] T.V. Nguyen, O.B. Yang, *Catal. Today* 87 (2003) 69–75.
- [64] Z. Zhang, J.T. Yates, *Chem. Rev.* 112 (2012) 5520–5551.
- [65] X.B. Chen, L. Liu, P.Y. Yu, S.S. Mao, *Science* 331 (2011) 746–750.
- [66] Y. Hou, F. Zuo, A. Dagg, P. Feng, *Angew. Chem. Int. Ed.* 52 (2013) 1248–1252.
- [67] K. Sivula, R. Zboril, F. Le Formal, R. Robert, A. Weidenkaff, J. Tucek, J. Frydrych, M. Grätzel, *J. Am. Chem. Soc.* 132 (2010) 7436–7444.
- [68] J. Kim, D. Monllor-Satoca, W. Choi, *Energy Environ. Sci.* 5 (2012) 7647–7656.
- [69] D.W. Kim, S.C. Riha, E.J. DeMarco, A.B.F. Martinson, O.K. Farha, J.T. Hupp, *ACS Nano* 8 (2014) 12199–12207.
- [70] T. Ling, M.K. Wu, K.Y. Niu, J. Yang, Z.M. Gao, J. Sun, X.W. Du, *J. Mater. Chem.* 21 (2011) 2883–2889.
- [71] O. Ovit, R. Tel-Vered, I. Baravik, O.I. Wilner, I. Willner, *J. Mater. Chem.* 19 (2009) 7650–7655.
- [72] N. Guijarro, T. Lana-Villarreal, R. Gomez, *Chem. Commun.* 48 (2012) 7681–7683.